

Controlling the coarsening dynamics of ferrogranular networks by means of a vertical magnetic field

Matthias Biersack , Ali Lakkis , and Reinhard Richter ^{*}
Experimentalphysik V, Universität Bayreuth, 95440 Bayreuth, Germany

Oksana Bilous [†], Pedro A. Sánchez , and Sofia S. Kantorovich 
University of Vienna, Faculty of Physics, Kolingasse 14-16, 1090 Vienna, Austria

 (Received 1 June 2023; accepted 16 October 2023; published 27 November 2023)

We are exploring in experiments the aggregation process in a shaken granular mixture of glass and magnetized steel beads, filled in a horizontal vessel, after the shaking amplitude is suddenly decreased. Then the magnetized beads form a transient network that coarsens in time into compact clusters, resembling a viscoelastic phase separation [Tanaka, *J. Phys.: Condens. Matter* **12**, R207 (2000)], where attached beads represent the slow phase. Here we investigate how a homogeneous magnetic field oriented in vertical direction impedes the emergence and growth of the networks. With increasing field amplitude this phase is replaced by a fluctuating arrangement of repelling, isolated steel beads. The experimental results are compared with those of computer simulations. Coarse-grained molecular dynamics confirms the impact of an applied magnetic field on the structural transitions and allows us to investigate long-time regimes and magnetic response not yet accessible in the experiment. It turns out that an applied magnetic field has different impacts, depending on its strength. It can be used either to slow down the dynamics of the structural transitions without changing the type of the resulting phases and only affecting the amount and sizes of clusters, or to fully impede the formation of network-like and compact aggregates of steel beads.

DOI: [10.1103/PhysRevE.108.054905](https://doi.org/10.1103/PhysRevE.108.054905)

I. INTRODUCTION

In a recent comment several “reincarnations of the phase separation problem” have been picked from the latest scientific literature [1]. One of the mechanisms highlighted by the authors is viscoelastic phase separation (VPS), proposed by Tanaka [2,3] for dynamically asymmetric mixtures, containing a fast and a slow component. Examples comprise suspensions of polymers in a much less viscous solvent, like water [4], or even biological cells [5,6]. The driving forces for the VPS are the differences in timescales of the constituents, commonly not taken into account in the standard models of phase separation [7–9]. The question arises of whether differences in timescales are also important if the slow phase just emerges during the transition.

This is the case for a granular mixture of glass and magnetized steel beads shaken in a horizontal vessel. After a sudden quench of the shaker amplitude, permanently magnetized steel beads “self-assemble” to dimers, or longer chains with a mobility, i.e., granular temperature, significantly lower than the surrounding gas of magnetic and glass spheres [10,11]. For a shallow quench soon compact crystallites of magnetized beads emerge [10]. In contrast, for a deep quench, the difference in mobility gives rise to the formation of transient networks, as shown in Fig. 1, which are coarsening in time to more compact clusters [12]. We have compared this transition with the morphology of VPS, comprising an initial

phase (here, chains), an elastic phase (governed by the elastic networks), and a hydrodynamic phase (made up by compact clusters) [12]. Whether this similarity is just a coincidence is yet not clear, because the model of VPS lacks so far universal features to be tested in the experiment.

To shed more light on the nature of the transition one would like to control the mobility of the different constituents prone to phase separation [13], “yet opportunities to manipulate it are surprisingly subtle and complex” [1]. In a first attempt the impact of an in-plane magnetic field onto phase separation of the ferrogranulate was studied in experiments and simulations [14]. Breaking the isotropy of the plain the resulting granular networks resembled those familiar from magnetorheological fluids [15,16] and standard [17,18] and inverse ferrofluids [19–21]. In contrast, in the present study, we preserve the isotropy of the system by means of an external field oriented orthogonally to the horizontal vessel. In this way the mobility of the jumping and rolling magnetized spheres is reduced. However, this is paid by additional complexity, namely the competition of dipolar attraction for horizontally aligned dipoles (known from the zero-field case), and a repulsion of dipoles oriented mutually in parallel to the applied field.

The magnetized steel beads utilized in the experiment are multidomain magnetic particles. In contrast to dipolar hard spheres—a standard model for single-domain magnetic nanoparticles—these spheres are also magnetically susceptible and have been termed susceptible dipolar hard spheres [14]. This feature has been found crucial to explain the formation of clusters different from chains [12]. This additional susceptibility, however, is rather difficult to model in computer simulations. Previously, we showed that as a simple

^{*}reinhard.richter@uni-bayreuth.de

[†]oksana.bilous@univie.ac.at

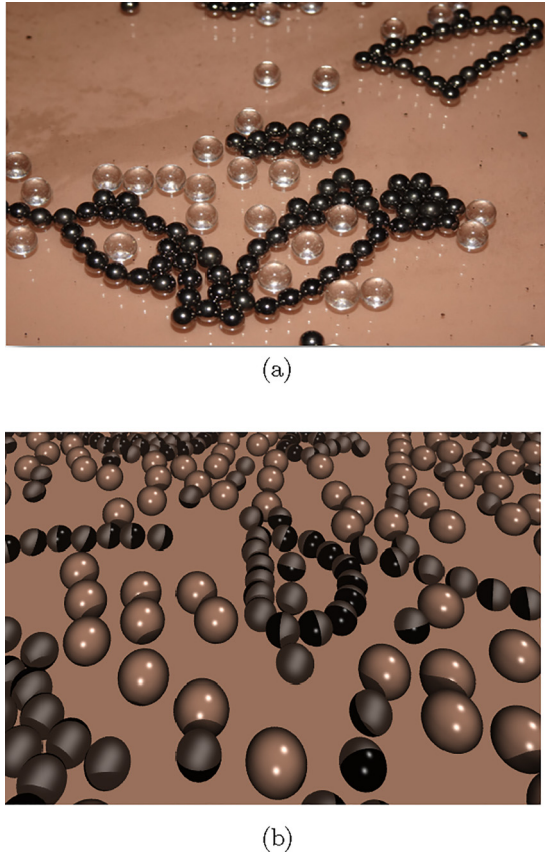


FIG. 1. Assembly of magnetized steel spheres: (a) in experiment; (b) in simulations. In (a) magnetic beads have dark solid color, and glass beads are transparent. In (b) the orientation of the magnetization is indicated by hemispheres of black and gray color.

approach one can use the combination of a single dipole and a central attraction [12]. An additional central attraction between the magnetic dipolar particles, in so-called Stockmayer fluids, results in a gas-liquid phase transition with particles forming droplet-like compact aggregates [22–26], instead of a familiar self-assembling into loose linear or branched clusters [27–33]. Even though a lot is known about phase behavior of Stockmayer fluids in bulk, the influence of a nonmagnetic component and geometrical constraints is still not analyzed in detail. In this study we employ this model and show that it can represent ferrogranulates fairly well even if an external magnetic field is applied.

This paper contains an experimental (Sec. II) and a numerical (Sec. III) part. In Sec. II A, we present the experimental setup, the materials used, the measurement protocol, and data extraction. In Sec. II B we present and discuss the results of the measurements, analyzing the structural evolution of the system. Next, in Sec. III A the simulation protocol is detailed. This is followed by the numerical results in Sec. III B. The paper ends with the summary of the main findings, given in Sec. IV.

II. EXPERIMENT

First we present the experimental methods (Sec. II A), which are followed by a report and discussion of the experimental results (Sec. II B).

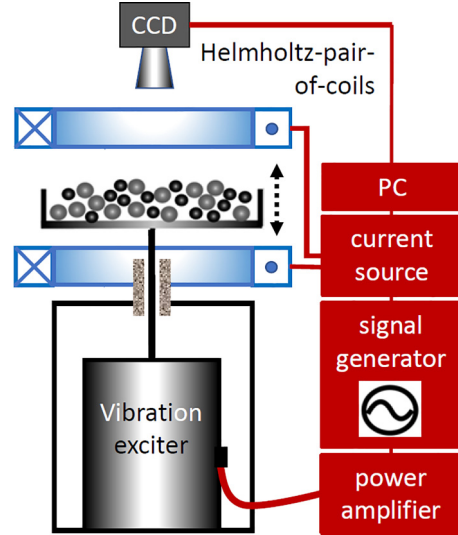


FIG. 2. Sketch of the experimental setup.

A. Experimental methods

In this section we describe the experimental setup, materials, measurement protocol, and data extraction.

1. Experimental setup

Our experimental setup is sketched in Fig. 2. An open vessel (width × length × height = 200 × 285 × 230 mm³) is mounted on top of a vibration exciter (Brüel & Kjær, type 4808) connected via an amplifier (Brüel & Kjær, type 2712) to a signal generator (Agilent, type 33120A). The latter generates a voltage which is sinusoidally varying in time, the amplitude and frequency of which can be controlled via a bus (GPIB) by a personal computer.

To reduce the magnetic stray field of the electromagnetic shaker the vessel is fixed via a hollow brass rod (diameter 20 mm) and a bearing and is situated 535 mm above the flange of the exciter. By previous measurements we could demonstrate that in this distance the stray field is comparable to the earth magnetic field [12].

A water-cooled Helmholtz pair of coils (marked blue in Fig. 2) serves to generate a magnetic induction B oriented orthogonal to the horizontal vessel. Each coil is connected to a current source (eurotest LAB/SL) controlled via GPIB by the computer. The applied magnetic induction B is recorded in the center of the coils by means of a Hall probe (Lakeshore, MMT-6J02-VH) connected to a teslometer (Lakeshore, Gaussmeter 450). Increasing the current from 0.00 A in 9 steps of 1.00 A yields the inductions

$$B_n = 0.231 \left[\frac{\text{mT}}{\text{A}} \right] \times n \times 1.00 [\text{A}] - 0.058 [\text{mT}], \quad (1)$$

with $n = \{0, 1, \dots, 8\}$. The negative offset, $B_0 = -0.058 \text{ mT}$, is introduced to take into account the earth magnetic field. During the experiments we record the acceleration amplitude Γ with an acceleration sensor (Brüel & Kjaer, type 4509 B002), which is mounted beneath the vessel.

TABLE I. Material properties of the utilized spheres.

Material	Steel	Glass
Supplier	ISOMetall	Sigmund Lindner
Type	DIN 1.3505 G10	P*
Radius (mm)	1.5	2.0
Precision (μm)	± 9.75	± 20
Mass (g)	0.108	0.084
Remanent moment m_r (10^{-4}Am^2)	1.8	

2. Spheres

Following Blair and Kudrolli [10] we use a mixture of steel and glass spheres. Their diameters and properties are listed in Table I. The steel spheres are magnetized in an electromagnet. For this purpose the spheres are inserted in a hexagonal grid of holes, as shown in Fig. 3, which are drilled in a plastic disk. The grid is closed by a lid, and then inserted in a 20 mm wide gap in between the cylindrical pole shoes (diameter 150 mm) of an electromagnet. In this way each sphere is magnetized by the same induction. The induction in the gap is increased from zero to 500 mT, and after one minute decreased to zero again. As shown in Ref. [12], the dipole moment of the spheres almost saturates at 500 mT. From the magnetization curve of the steel spheres (see Fig. 6 in Ref. [12]) we can estimate the dipole moment of a steel sphere in the applied induction B to

$$\vec{m}(B) = a \cdot \vec{B} + \vec{m}_r, \quad (2)$$

where $a = 3.27 \times 10^{-2} \text{ Am}^2 \text{ T}^{-1}$ is determined by the susceptibility of the steel, and m_r is the remanent dipole moment (cf. Table I) at $B = 0.0 \text{ mT}$ [34,35].

The filling fraction ϕ of both types of spheres is defined via

$$\phi = N \frac{A_{\text{hex}}}{A_{\text{vessel}}} = N \frac{2\sqrt{3} r_{\text{sphere}}^2}{A_{\text{vessel}}}, \quad (3)$$

where N counts the number of spheres, A_{hex} captures the area of the regular hexagon around a sphere of radius r_{sphere} , and $A_{\text{vessel}} = 5.7 \times 10^4 \text{ mm}^2$. In this way ϕ becomes 1 for a hexagonal close packing in 2D [10] (note that there is a typo



FIG. 3. Hexagonal grid of holes filled by steel spheres. The diameter of the disk is 150 mm; its thickness, including a lid, is 20 mm.

in Eq. (3) of Ref. [12]). For all measurements reported here we selected $N_g = 473$ glass spheres and $N_s = 841$ steel spheres, which yields for both types of spheres an area filling fraction of $\phi_g = \phi_s = 0.115$.

3. Measurement protocol

Each series of measurements is performed in the following way. First, the acceleration amplitude is switched at $t = -60 \text{ s}$ to $\Gamma_{\text{gas}} = 3.3 \text{ g}$, which is sufficient to generate a homogeneous granular gas. At $t_B = -5.0 \text{ s}$ the magnetic induction is switched from B_0 to a selected value B_n , given by (1). At $t_q = 0 \text{ s}$, when the field had ample time for its buildup, the acceleration is quenched to $\Gamma_q = 1.8 \text{ g}$ and the evolution of the pattern is recorded with a CCD camera for 120 s. To obtain reliable statistics, this sequence is repeated 50 times for each selected induction B_n .

4. Image processing and data extraction

In order to be able to analyze the networks of steel spheres we apply the following image processing and data extraction procedure to the recorded frames. First, a trapezoid correction is applied to the images, followed by a binarization. For a proper detection of all spheres, the binarization threshold needs to be increased in steps. These binary images are then processed with tools from the computer vision software OpenCV [36] which yields the contour and coordinates of the spheres. Next, for the identification of the networks, neighboring spheres have to be recognized. In order to do this, the center-to-center distance of each pair of spheres is compared with their diameter, $2r_{\text{sphere}}$. The topology of the networks is reduced to a graph (see, e.g., Fig. 13 of Ref. [12]) by means of the software package networkX [37] based on the script language Python [38].

B. Experimental results and discussion

Here we present the experimental results, starting with a visual inspection of the structures of the networks of magnetic beads (Sec. II B 1) followed by their formal analysis based on the distributions and averages of the number of neighbors (Sec. II B 2).

1. Evolution of the structures

Figure 4 presents an overview of the evolution of the networks of magnetic beads for three representative times [left to right: columns (a) to (c)] and three representative magnetic fields [top to bottom: rows (1) to (3)]. For minimal magnetic induction, B_0 , panel (a1) displays emerging chains and small clusters already 5 s after the quench, which have developed to larger networks after 25 s (b1). During the next 75 s this process continues more slowly which yields a network percolating from the left to right of the vessel, and some more compact clusters (c1). At intermediate magnetic induction, B_4 , we observe after 5 s (a2) smaller chains, when compared with (a1); at 25 s (b2) the chains are less compact, and at 100 s (c2) the clusters are less extended, when compared with (c1). Obviously B delays the evolution from chains, via networks, to clusters. This becomes even more evident at a large magnetic induction, B_8 . In panel (a3) we see only individual

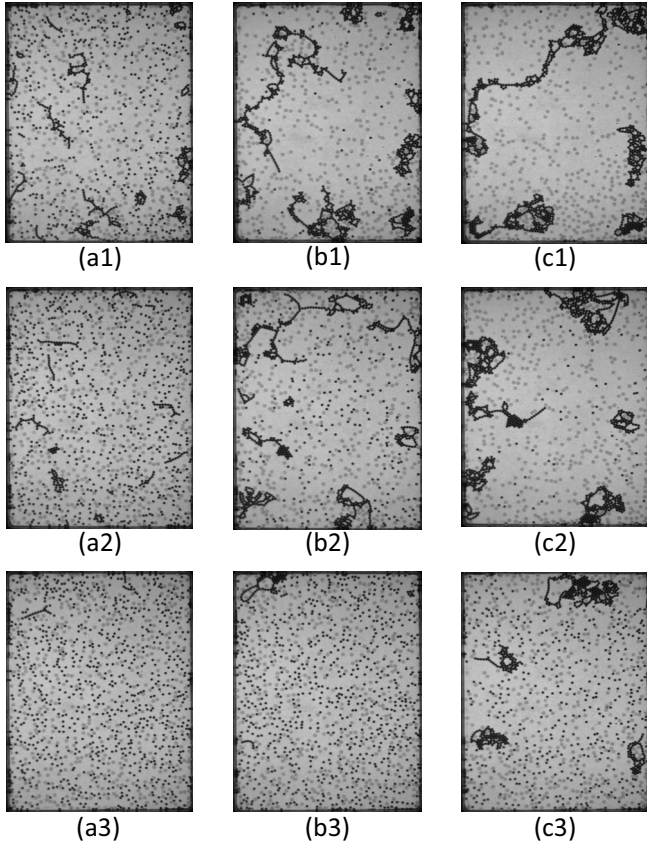


FIG. 4. Examples of configuration snapshots for B_0 (1), B_4 (2), and B_8 (3) at 5 s (a), 25 s (b), and 100 s (c) after the quench. See also the related movies B0.mp4, B4.mp4, and B7.mp4 that we have made available [45].

steel spheres, which can hardly develop networks (b3). Those appear only very late (c3). Inspecting panel (c3) more carefully, we can discriminate besides the clusters a large number of individual steel spheres. Apparently this phase coexists with the clusters. Let us now analyze the pattern evolution by means of network quantities.

2. Number of neighbors

The topology of the clusters formed by the magnetic beads can be represented as a network, in which each bead corresponds to a node and the close contact connections between pairs of beads are represented by edges. Thus, in this description the number of edges of each node—often addressed as its *degree*, k —represents the number of neighbors of the corresponding bead. A fundamental property of a network is its distribution of degrees, which in our case can help to identify the dominant structures in the system. In a chainlike structure beads have two neighbors, $k = 2$, except those at the chain ends, which have only one, $k = 1$. In a two-dimensional system k is limited geometrically to 6, corresponding to a hexagonal close packing. In the following, we define the fraction of nodes with degree k , F_k , as

$$F_k = \frac{n_k}{N_S}, \quad k = \{0, 1, \dots, 6\}, \quad (4)$$

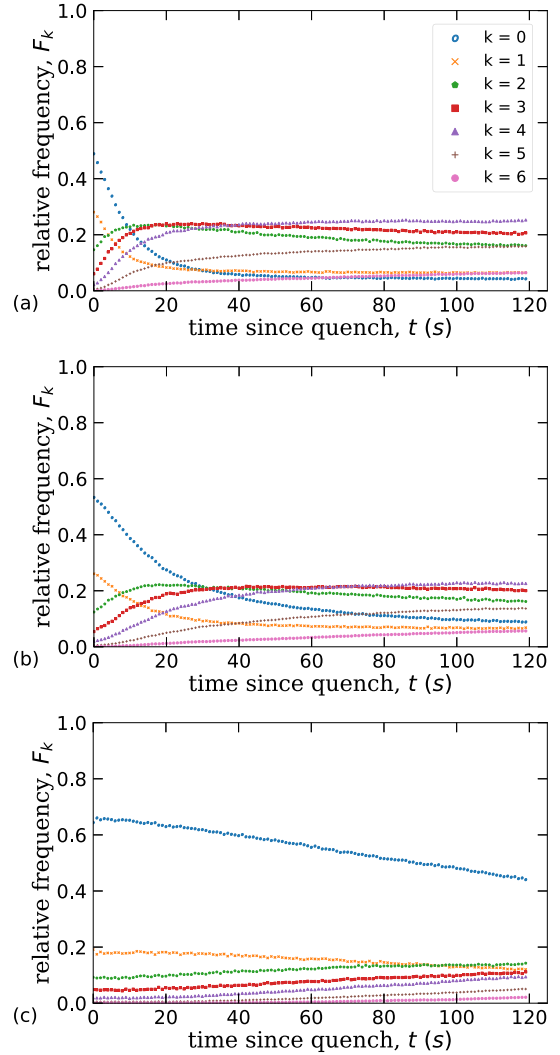


FIG. 5. Time evolution of F_k (4). The magnetic induction B is kept constant in each run, but increases from B_0 (a) via B_4 (b) to B_8 (c). The legend in panel (a) applies to the three plots.

where n_k is the number of steel spheres with k neighbors and N_S is the total number of steel spheres in the system. Thus, this parameter represents the probability of a magnetic bead to have a number of neighbors k .

The time evolution of the different fractions F_k is plotted in Fig. 5 for the same selected values of magnetic induction that were presented in Fig. 4. For minimal field, B_0 [panel (a)], one sees a drastic decay of F_0 (blue \circ), and F_1 (orange \times), which represent isolated beads and loose edges of chains, respectively. F_2 (green pentagons), F_3 (red squares), and F_4 (purple triangles), corresponding to linear chains and intermediate compact cluster regions, are first increasing and later slowly decreasing, when highly compact clusters, captured by F_5 (brown crosses) and F_6 (pink solid circles), become prominent. The situation is similar for intermediate magnetic induction, B_4 , as displayed in Fig. 5(b). However, in this case F_0 decays more slowly. Figure 5(c) presents the evolution of the node degrees at maximum applied induction, B_8 . Isolated steel spheres are now the dominant phase throughout the whole sampled time interval, and F_0 decays almost linearly

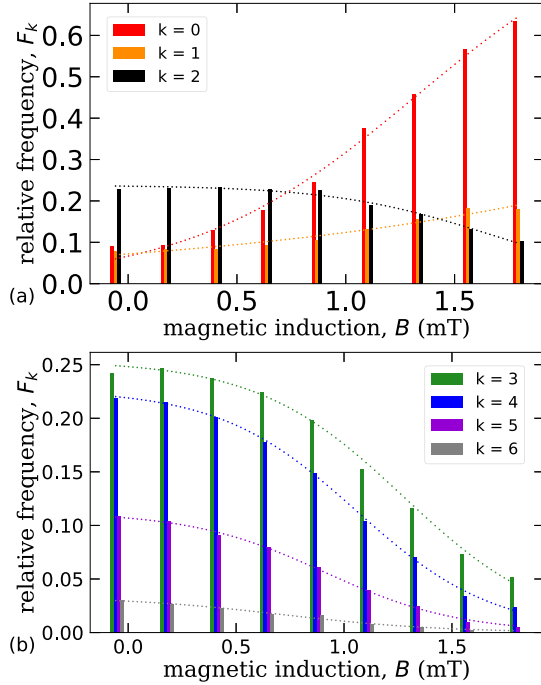


FIG. 6. Relative frequency of the number of neighbors versus the applied magnetic induction B , recorded 25 s after the quench. For clarity, panel (a) displays only F_0 (red), F_1 (orange), and F_2 (black). Panel (b) is devoted to F_3 (green), F_4 (blue), F_5 (purple), and F_6 (gray). To guide the eyes the evolution of the different fractions with B have been fitted by the function (dotted line) $F_k(B) = a\{1 + \exp[-b(B + B_c)]\}^{-1}$, where a scales the amplitude, b is the growth rate, and B_c an offset.

at a low rate. The decay of F_1 is even weaker, whereas contributions of F_2 to F_6 , capturing chains, loose networks, and compact clusters, are also very slowly increasing.

In order to better visualize the effects of the induction on the formation of aggregates, we present in Fig. 6 the fractions F_k observed at time $t = 25$ s as a function of B_n . It represents a “vertical cut” through Fig. 5 at a time that corresponds to the central column [(b1)–(b3)] in Fig. 4. This time roughly signals the end of the fast early variations of F_k observed at low and moderate inductions. To ease the visualization, the results are split into panel (a), which shows the evolution for $k = \{0, 1, 2\}$, and panel (b), for $k = \{3, \dots, 6\}$. The fraction which is most prominently increasing with B is F_0 (red) as shown in (a). This is in agreement with the visual inspection of the snapshots displayed in Fig. 4 [central row: (a2), (b2), (c2)], indicating that with increasing B more and more steel spheres remain disconnected. F_1 (orange), characterizing the fraction of dimers and chain ends, is only slightly increasing. The black bars mark F_2 , characteristic for beads embedded in chains and rings. This fraction is diminishing with B , indicating that beads which are part of in-plane head-to-tail dipolar configurations, have more difficulties to form with increasing B .

Figure 6(b) displays a prominent decay of *all* fractions for $k > 2$ with increasing B . This is in agreement with the inhibition of the cluster growth produced by B . A particularly characteristic fraction is F_6 (marked in gray), which decays

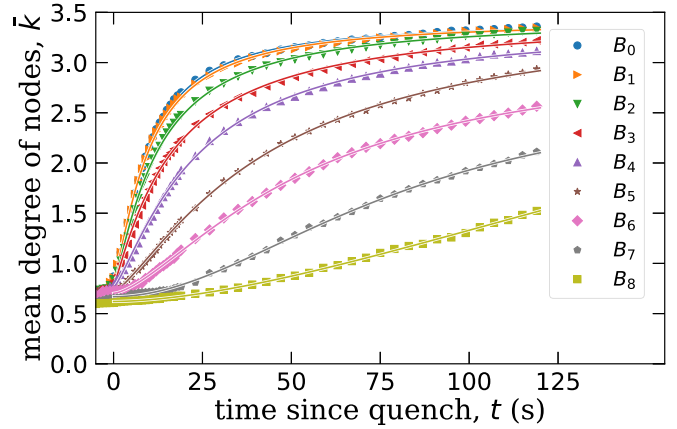


FIG. 7. Temporal evolution of the mean degree of the nodes for different applied magnetic inductions B_n , as listed in Table II. To not overload the graphs, for $t > 20$ s only every 4th data point has been plotted.

by a factor of 43 to $F_6(B_6) = 1 \times 10^{-3}$, indicating that for $N_s = 841$ less than one sphere has six neighbors, on average.

A compact overview of the complex network evolution can be gained from the mean number of neighbors, \bar{k} , that we can define as

$$\bar{k} = \frac{\sum_{k=0}^6 kn_k}{N_s} = \sum_{k=0}^6 kF_k. \quad (5)$$

The evolution of $\bar{k}(t, B)$ is plotted in Fig. 7. Consistently with the observations for F_k , for minimal induction, B_0 , one can discriminate two regimes. In the initial regime, which lasts about 25 s, we observe a fast increase of \bar{k} , which is correlated with the formation of chains in Fig. 4. After that, the clusters evolve to form more compact structures, making \bar{k} to increase more slowly. Those two regimes are the parts of a similar process but are characterized by quantitatively different dynamics. Indeed, the temporal evolution of \bar{k} can well be fitted by a common function for both regimes. It is the sigmoidal growth function

$$\bar{k}(t) = \bar{k}_{\text{ini}} + \bar{k}_{\text{gro}} \left(1 - \frac{1}{1 + \left(\frac{t}{t_{1/2}}\right)^p} \right), \quad (6)$$

that describes diverse limited growth processes in nature [39]. Here, \bar{k}_{ini} denotes an offset, already present at $t < 0$ s, which characterizes short time contacts during the collisions of spheres. The maximal growth is marked by \bar{k}_{gro} . Moreover, $t_{1/2}$ denotes the half-value period when $\bar{k}(t_{1/2}) = \frac{1}{2}(\bar{k}_{\text{gro}} - \bar{k}_{\text{ini}})$, and p is a scaling exponent, which captures the curvature of the graph. Only for B_8 the gradual increase does not provide enough data for a reliable fit. The fitting parameters are listed in Table II.

The curves in Fig. 7 show that with higher fields the growth of \bar{k} becomes increasingly slower. Consequently, the fits by (6) yield slightly lower values for \bar{k}_{gro} (Table II, 4th column). The retardation of the network evolution is most prominently captured by the half-value period $t_{1/2}(B)$, as marked in Fig. 8 by blue circles. The first slow, then rapid increase of $t_{1/2}(B)$

TABLE II. The table displays B_n according to (1). A fit of (6) to the data for the mean degree of a node \bar{k} , as displayed in Fig. 7, yields the parameters displayed in columns 3 to 6.

B_n	(mT)	\bar{k}_{ini}	\bar{k}_{gro}	$t_{1/2}$ (s)	p
B_0	-0.058	0.84	2.57	9.64	1.37
B_1	0.174	0.84	2.58	9.97	1.32
B_2	0.405	0.79	2.66	12.37	1.23
B_3	0.636	0.77	2.70	16.63	1.13
B_4	0.867	0.76	2.65	23.65	1.26
B_5	1.099	0.71	2.81	44.03	1.30
B_6	1.330	0.70	2.41	54.14	1.49
B_7	1.561	0.67	2.12	81.92	1.94
B_8	1.793				

can be well described by an exponential function

$$t_{1/2}(B) = t_1 \exp\left(\frac{B}{B_e}\right) + t_2, \quad (7)$$

with $t_1 = (5.7 \pm 2.5)$ s, $B_e = (0.59 \pm 0.07)$ mT, and the offset $t_2 = (1.9 \pm 4.3)$ s. Note that (7) predicts $t_{1/2} = 1$ h for an induction of $B = 3.8$ mT, only.

So far, we could show that the coarsening dynamics of ferroganular networks in a plane can well be characterized by the mean number of neighbors, $\bar{k}(t, B)$. This order parameter exhibits a sigmoidal growth (6) that slows down considerably with growing magnetic induction perpendicular to the plane.

III. COMPUTER SIMULATIONS

Experimental results evidence the impact of an applied magnetic field on the structural transformations in a shaken ferroganulate mixture, particularly in the first and the second dynamic regimes. It is, however, not feasible to elucidate quantitatively in experiments the long-time behavior as it is not possible to fully exclude finite-size effects. Simulations, in contrast, allow us to avoid the aforementioned limitations, albeit in a simpler, more coarse-grained model. Below, we first introduce such a model and the simulation protocol; next, we

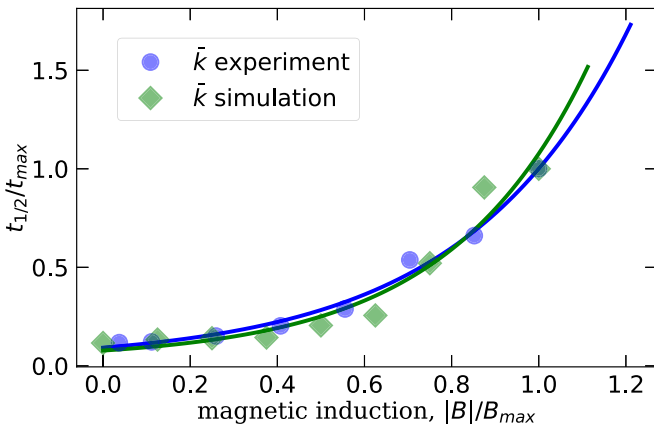


FIG. 8. Half-value period $t_{1/2}(B)$ for experimental (blue circles) and numerical (green diamonds) data, as displayed in Tables II and III, respectively. The solid line marks a fit by (7).

discuss the findings and focus on two main points: first, we justify why the model is applicable for the systems investigated in experiments; second, we analyze the orientations of particle magnetization and the system magnetic response during the structural transformations. The latter adds an insight that experimentally is not yet accessible.

A. Simulation protocol

We employ Langevin dynamics simulations [12,14], treating ferroganulate as a two-component mixture. Simulations are performed with the ESPResSo 4.1.4 simulation package. The glass component is represented by purely repulsive spheres with diameter σ_g , interacting via the Weeks-Chandler-Andersen potential:

$$u_{\text{WCA}} = \begin{cases} u_{\text{LJ}}(r_{ij}) - u_{\text{LJ}}(r_{\text{cut}}), & r_{ij} < r_{\text{cut}}, \\ 0, & r_{ij} \geq r_{\text{cut}}, \end{cases} \quad (8)$$

where $|\vec{r}_{ij}| = r_{ij}$ is the modulus vector between centers of spheres i and j , and u_{LJ} is a standard Lennard-Jones potential, given by (9), with the depth of its well ε ,

$$u_{\text{LJ}} = -4\varepsilon \left[\left(\frac{\sigma_g}{r_{ij}}\right)^{12} - \left(\frac{\sigma_g}{r_{ij}}\right)^6 \right]. \quad (9)$$

By taking $r_{\text{cut}} = 2^{1/6}\sigma_g$, the potential (8) becomes purely repulsive. The second component is a classical Stockmayer system in which two particles i and j , with identical diameters σ_m , interact via an attractive u_{LJ} , represented by (9) with σ_g being replaced by σ_m . Additionally, particles i and j possess magnetic moments \vec{m}_i and \vec{m}_j that are interacting via the dipole-dipole potential

$$u_{ij}^{\text{dd}} = -\frac{\mu_0}{4\pi} \left[3 \frac{(\vec{m}_i \cdot \vec{r}_{ij})(\vec{m}_j \cdot \vec{r}_{ij})}{r_{ij}^5} - \frac{\vec{m}_i \cdot \vec{m}_j}{r_{ij}^3} \right], \quad (10)$$

where μ_0 is the magnetic permeability of vacuum. In this way we build a minimal phenomenological representation of the magnetic interaction of the steel beads, which have a permanent dipole moment and are as well magnetically susceptible [12].

The trajectories of all particles are obtained by solving Langevin equations in quasi-2D: particle centers are constrained to one plane, but rotations are allowed in all three dimensions. The system in simulations is made pseudoinfinite via lateral periodic boundaries. The thermal noise of the Langevin thermostat in simulations serves to model the effects of the mechanical shaker; thus, the experimental shaking amplitude corresponds to the system temperature. As a result, in simulations, the quenching is performed by a sudden decrease of the system temperature. The Weeks-Chandler-Andersen potential is used to model as well the repulsion between glass and magnetic beads with an effective diameter $\sigma = (\sigma_m + \sigma_g)/2$ and $r_{\text{cut}} = 2^{1/6}\sigma$ accordingly. In both cases the energy scale of the potential is set to unity.

In simulations, similarly to the experiment described above (cf. Table I), area fractions of magnetic and glass spheres were $\phi_m = 0.1$ and $\phi_g = 0.1$ with dimensionless diameters $\sigma_g = 4$ and $\sigma_m = 3$. The dimensionless temperature before quenching is $T_1 = 5$, and after quenching, $T_2 = 0.5$. The conventional

TABLE III. The table displays in the magnetic inductions B_n^* , impressed in the simulations together with the parameters obtained by a fit of (6) (short-time regime) to the numerical data of $\bar{k}(t)$, displayed in Fig. 10.

B_n^*	(s.u.)	\bar{k}_{ini}	\bar{k}_{gro}	$t_{1/2}^*$ (s.u.)	p^*
B_0^*	0.0	0.4	1.72	12.34	0.81
B_1^*	0.1	0.38	1.81	14.19	0.72
B_2^*	0.2	0.39	1.74	14.94	0.76
B_3^*	0.3	0.39	1.63	15.32	0.83
B_4^*	0.4	0.4	1.57	21.85	0.81
B_5^*	0.5	0.4	1.37	27.25	0.87
B_6^*	0.6	0.39	1.3	55.47	0.76
B_7^*	0.7	0.38	0.97	96.46	0.93
B_8^*	0.8	0.36	0.36	106.52	1.77

measure of the strength of the dipole-dipole interaction becomes then $\lambda = m_i^2/T_1\sigma_m^3 = 5$. We chose $\varepsilon = 0.5$ for the strength of the isotropic attraction, as it provided the closest structural resemblance to the experiment in the previous studies [12,14]. These values were obtained by placing $N_m = 814$, $N_g = 458$ spheres in a square simulation box with side length of $L = 240$.

First, the beads are randomly placed within the simulation box and the system is equilibrated at a temperature, T_1 , which is sufficiently high to maintain a gaslike state. For the gas phase, simulation runs consisted of 12×10^4 integrations at T_1 with a simulation time step of $\delta t_1 = 0.005$.

Second, we perform a quenching process by abruptly reducing the temperature to its final value, T_2 , and switching on the external field perpendicular to the layer of particles. The magnetic field applied in the simulations is denoted as \vec{B}_n^* , where $*$ is used to distinguish it from the experimental one and underline its dimensionless nature (cf. Table III). The applied field introduces a new interaction in the simulation model, represented by the Zeeman potential acting on each magnetized particle i according to its corresponding dipole, \vec{m}_i , via

$$u_i^z = -\mu_0(\vec{m}_i \cdot \vec{B}_n^*). \quad (11)$$

In this work we investigate the range of the field strength $B_n^* = |\vec{B}_n^*| \in [0, 0.8]$ for eight different dimensionless field values with equal intervals of 0.1, for which we observe behaviors qualitatively comparable to the ones found in experiments. Note that here we do not aim at any quantitative description of the experiment; rather we focus on the qualitative trends and the avoidance of the finite-size effects caused by the vessel walls in the experiment.

Long-range magnetic interactions were calculated, using the dipolar P3M algorithm with dipolar layer correction [40,41].

After quenching the time step is fixed to $\delta t_2 = 0.0005$. Performing several preparatory runs in a zero magnetic field, it was found that there are three characteristic regimes: the first two that are related to the same process are the *initial* one, where the observables are changing rapidly and the transformation from the gas phase to self-assembled chains occurs, and the *intermediate regime*, in which the networks are evol-

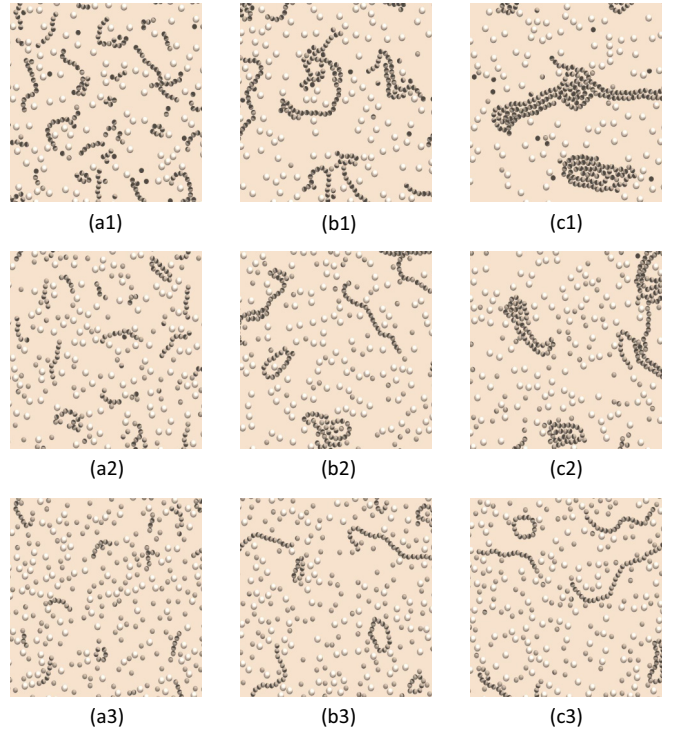


FIG. 9. Simulation snapshots corresponding to three different times of our simulation, which are, from left to right, (a) initial $t = 17$ s.u., (b) intermediate $t = 48$ s.u., and (c) long time (the very last configuration saved). The applied external magnetic field is increased (from top to bottom). Horizontally, (a1), (b1), (c1) $|\vec{B}_0^*| = 0.0$; (a2), (b2), (c2) $|\vec{B}_5^*| = 0.5$; (a3), (b3), (c3) $|\vec{B}_8^*| = 0.8$ in simulation units. Vertically, (a1), (a2), (a3)—shortly after quenching that matches the initial regime; (b1), (b2), (b3)—the last snapshot of the intermediate regime; (c1), (c2), (c3)—the last time instance of the simulation. See also the related movies Hz 0.0.mpg, Hz 0.5.mpg, and Hz 0.8.mpg that we have made available [45].

ing; finally, there is the long-time regime, in which clusters merge. Based on these observations we changed the frequency of sampling. During the first 4×10^5 integrations, we record the configurations every 10^4 steps. This allows us to resolve fast dynamics in the initial and intermediate regimes. After that, during the last 12×10^6 integrations, we only record every 10^6 steps.

B. Numerical results and discussion

Analogously to the discussion of the experimental results, we present here the numerical results, starting with a visual inspection of the structures of the networks of magnetic beads (Sec. III B 1). This is followed by their formal analysis based on the averages of the number of neighbors (Sec. III B 2). Finally, we extend the analysis by studying the magnetization along the z axis (Sec. III B 3).

1. Evolution of the structures

We start the discussion of the numerical results by visual inspection of the simulation snapshots displayed in Fig. 9 for three different values of $|\vec{B}_n^*|$ and for three different times: initial (a), intermediate (b), and long time (c).

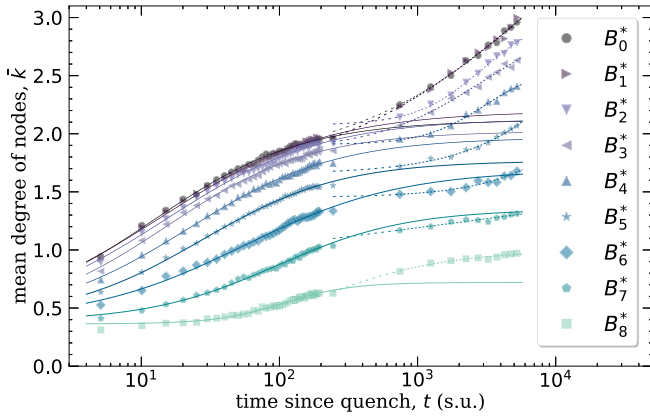


FIG. 10. Mean degree of a node versus simulation time for different applied magnetic fields B_n^* , listed in Table III. The symbols mark the data estimated from the simulation results. The solid (dashed) lines indicate fits by (6) for $t \in [5, 195]$ ($t \in [744, 6244]$).

Each of the three rows in Fig. 9 corresponds to a certain value of the magnetic induction, namely B_0^* , B_5^* , and B_8^* in simulation units (s.u.). Hence, in the first row (1) without an applied field, many clusters form rapidly, showing time-dependent merging with subsequent formation of compact islands, connected by linear segments. By taking a closer look, the orientation of the magnetic dipoles of the particles can be unveiled since the north (south) of the dipoles have been marked black (brown).

In the remainder of Fig. 9 the system undergoes a temporal evolution, which is different from the one observed in the first row in zero fields and investigated before [12]. For a moderate field of B_5^* , displayed in Fig. 9, panels (a2)–(c2), the size of the emerging structures is diminished, and many solitary magnetic beads remain. This tendency is clearly reinforced at the highest value of $|B_8^*| = 0.8$, as shown in Fig. 9, panels (a3)–(c3). Here, no compact clusters are found even for the last simulation configuration, presented in Fig. 9, panel (c3).

After confirming similarities for the pattern evolution of ferrogranulate under the influence of an applied magnetic field in the simulations and experiments, we proceed with a comparison of the main observables in order to justify the choice of the model parameters and obtain an extra insight in the magnetic response.

2. Number of neighbors

First, we calculate the mean number of nearest neighbors, \bar{k} , of each magnetic particle, and plot them as functions of time in Fig. 10. This is done for each value of the magnetic induction considered in the simulations. Different colors and shapes of the symbols correspond to different intensities of an applied external field, as detailed in Table III. Unless specified otherwise, the size of the symbols in simulations corresponds to the largest error bars.

The plots in Fig. 10 are directly comparable to the experimental findings in Fig. 7. Looking at $\bar{k}(t)$, we can clearly discern two qualitatively different processes. The first process is characterized by the first and the second time regimes, that corresponds to simulation times below 2×10^2 and is the same as in the experiment, shown in Fig. 7. It is qualitatively

similar for all values of B_n^* . Namely, the short and intermediate time behavior is well characterized by the sigmoidal growth function (6), already describing successfully the experiment. The values obtained from the fits are collected in Table III.

If we compare the fitting parameters to those found in the experiment and provided in Table II, we find the numerical ones to be consistently lower, albeit with the same qualitative behavior. The lower values of \bar{k}_{ini} and \bar{k}_{gro} can be attributed to the finite-size effects present in the experiment. As for the differences in the values of $t_{1/2}^*$, they simply indicate the scaling factor between simulation and experimental time units. On the other hand, the proximity of the exponents, found in numerical (p^*) and in experimental (p) data, underline a full qualitative agreement between both approaches and suggest that the mean number of neighbors each magnetic particle has rapidly decreases with the growth of an applied magnetic field. The similar pattern evolution is reconfirmed when inspecting the half-value period $t_{1/2}(B)$ as plotted in Fig. 8. This means that regardless of coarse-graining of magnetic interactions, the simulation approach reproduces the short-time growth of \bar{k} accurately.

For long times the sigmoidal growth of $\bar{k}(t)$ deviates considerably from the predictions of (6) when fitted to the short-time regime. As an *ad hoc* approach we fit the numerical data by (6) but restrict the data to the long-time regime. Even though the results (marked in Fig. 10 by dashed lines) appear at a first glance reasonable, the strongly varying fitting parameters (see Table IV) suggest that (6) has in the long-time regime no predictive power. While \bar{k}_{ini} , \bar{k}_{gro} , and p^* scatter considerably, $t_{1/2}^*$ appears only mildly affected by B^* . This may be interpreted in this way, that once the magnetized beads have formed head-to-tail chains and clusters, their coarsening is hardly affected by B^* . Inspecting this evolution more carefully for different values of the applied field, we see that for $B_n^* < 0.5$, the growth is fast with no signs of saturation. Once $B_n^* > 0.6$, the convexity of \bar{k} changes and the growth becomes notably slower. All in all, the long-time regime differs considerably from the initial and intermediate ones, and may characterize a physically different evolution process, like the hydrodynamic regime in VPS.

Even though we cannot directly compare the third time regime to the experiment, an excellent agreement for the values of \bar{k} in experiment and simulation in the first two regimes reassures the predictive potential of the simulation approach. This is at least true for the coarsening dynamics of a symmetric mixture of steel and glass beads, namely $\phi_g = \phi_s = 0.1$.

This justifies exploring, just *in silico*, the impact of an asymmetric mixture, because the experiments are rather tedious. Keeping the total filling fraction to $\phi = \phi_g + \phi_s = 0.2$, we have simulated the coarsening for an enriched ($\phi_s = 0.15$), a symmetric ($\phi_s = 0.10 = \phi_g$), and a depleted ($\phi_s = 0.05$) mixture of magnetized steel and glass beads, as shown in Fig. 11. Here, $\bar{k}(t)$ is plotted for three representative values of the magnetic induction, namely B_0^* (a), B_5^* (b), and B_8^* (c). In each case, the magnetically enriched mixture (full circles) has the highest value for \bar{k} , then follows the symmetric mixture (half-filled circles), and eventually the magnetic depleted mixture (open circles). The solid lines in Fig. 11 mark fits by (6) in the short-time regime, with the fitting parameters

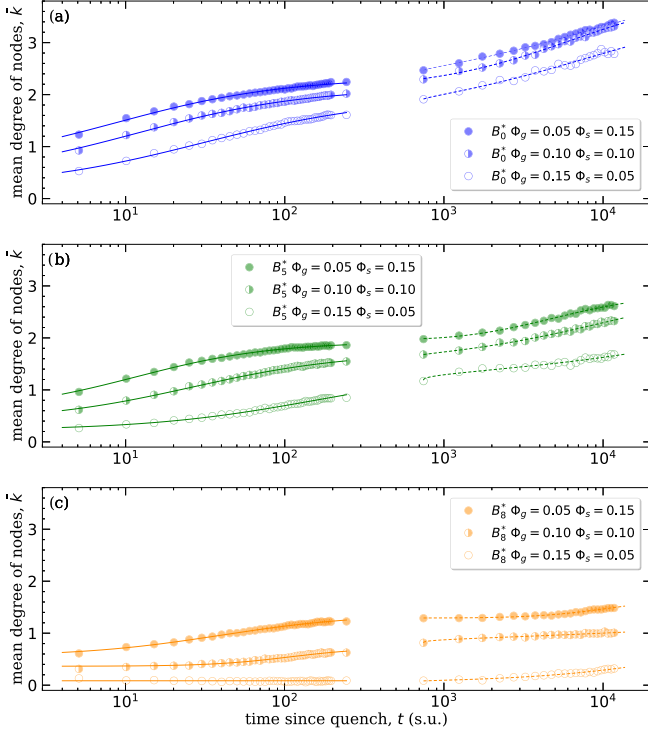


FIG. 11. Mean degree of a node versus simulation time, for the total filling fraction $\phi = 0.2$ with $\phi_s = 0.05$ and $\phi_g = 0.15$ (filled circles), three different mixtures with depleted, symmetric, and enriched magnetic content, and (a) B_0^* , (b) B_5^* , (c) B_8^* . Fits by (6) for $t \in [5, 195]$ ($t \in [744, 11744]$) are indicated by solid (dashed) lines. The fitting parameters for the short (long) regime are given in Table V (Table VI).

presented in Table V. For B_0^* the absolute growth, \bar{k}_{gro} , as well as the growth exponent, p^* , hardly depend on ϕ_s . In contrast, the half-value time, $t_{1/2}$, increases considerably with decreasing magnetic filling fraction ϕ_s , in accordance with the reduced probability to meet another steel bead. The situation is similar for B_5^* . For B_8^* we observe a drastic increase of $t_{1/2}$ with decreasing ϕ_s , but \bar{k}_{gro} and p^* vary considerably. At those high inductions one has to be cautious with the validity of the phenomenological Eq. (6), as we have seen already in the experiment (cf. Fig. 7). To summarize, in the short-time regime, the scaling of $\bar{k}^*(B^*, \phi)$ is met fairly well by the phenomenological growth function (6) for all three mixtures studied.

Let us now turn to the long-time regime, displayed on the right of Fig. 11. Once again, the numerical results deviate considerably from the predictions of (6), when fitted to the short-time regime. Table VI displays the strongly varying fitting parameters. As in the short-time regime, a decrease of the magnetic fraction is lowering \bar{k} considerably. This becomes most prominent in Fig. 11(c).

At this point, it can safely be said that the simulation model is capable of capturing the dynamics of structural transformations and can be used not only to analyze long-time behavior, and mixtures so far not available experimentally. The same is true for order parameters different from the mean number of neighbors \bar{k} .

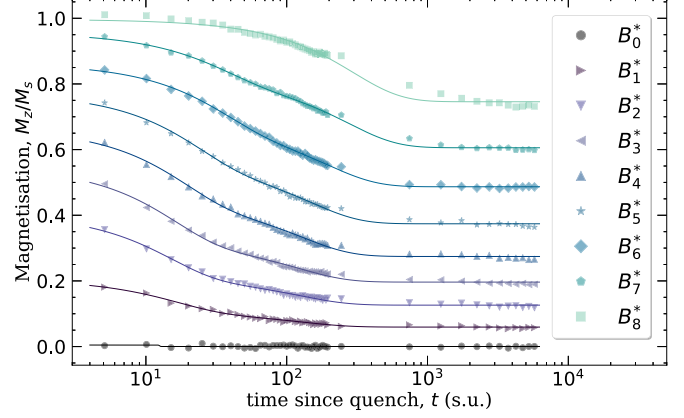


FIG. 12. Magnetization along z versus the simulation time for the different values of the impressed field B_n^* (Table III). The solid lines indicate fits by the bi-logistic growth function (12).

3. Magnetization

One of those order parameters is the magnetization of the total system, i.e., the projection of the system magnetic moment onto the field direction, M_z . Its time dependence is plotted in Fig. 12, where the values are normalized by the saturation magnetization M_s of the system.

Here, similarly to Fig. 10, we observe two distinct processes characterized by three time regimes. The fact that the ranges, corresponding to each of them, coincide for \bar{k} and M_z/M_s evidences that structural transformations and changes in the magnetic response are synchronous.

Immediately after the quench, while the particles have yet not agglomerated, the system gets rapidly magnetized, particularly if the field is high. However, as time passes, the formation of clusters inevitably leads to the reduction of M_z/M_s , as the neighboring particles in clusters assume head-to-tail orientations in the plane, i.e., orthogonal to an applied field. Eventually $M_z/M_s \equiv \hat{M}_z$ saturates at $\sum_{i=0}^2 \hat{M}_i(B)$. For simplicity the relaxation of the magnetization is captured by a bi-logistic growth [42] (here decay) function

$$\hat{M}_z = \hat{M}_0 + \frac{\hat{M}_1}{1 + e^{-\frac{\ln 81}{\Delta t_1}(t-t_{m1})}} + \frac{\hat{M}_2}{1 + e^{-\frac{\ln 81}{\Delta t_2}(t-t_{m2})}}. \quad (12)$$

Here k_i ($i = 1, 2$) denotes the coefficient of the i th growth function, Δt_i the characteristic duration for a growth (decay) from 10% to 90%, and t_{mi} the time when the midpoint is reached by the i th growth trajectory. The fits by (12) are marked in Fig. 12 by solid lines.

In the long-time regime, interestingly enough, the magnetization does not change anymore. However, this saturation level depends on the value of the applied induction B^* .

This means that the further growth of clusters, characterized by an increase of $\bar{k}(t)$ (cf. Fig. 10), is not accompanied by the orientation changes in the particle magnetic moments. Thus, if there is no gain in Zeeman energy (11), one would expect the structural transformations to occur through a different mechanism.

In order to look closer at the initial response of the system to an applied magnetic field and zoom in on the initial reaction of the system on the applied field in Fig. 12, we calculated the

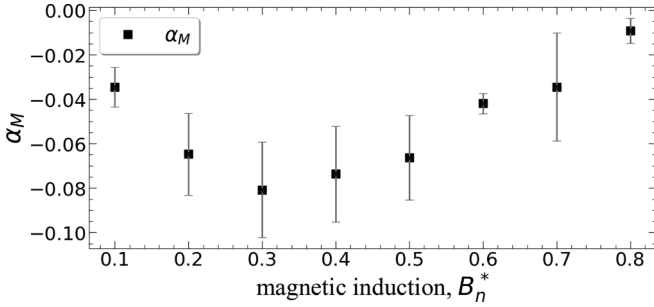


FIG. 13. The initial decay rate for the magnetization, $\alpha_M = \partial M_z / \partial t$, versus the magnetic induction B_n^* .

time derivatives of the magnetization, $\alpha_M = \partial M_z / \partial t$, using the first three data points. The error bars related to numerical differentiation are provided by vertical lines.

Judging from the rate with which the magnetization of the system decays with growing applied magnetic field, α_M , shown in Fig. 13, we observe that initially the rate of decay becomes more negative, but once an external magnetic field reaches B_3^* (Table III), the decay rate reaches its minimum, and starts increasing again.

The value of B_3^* can be considered the highest if we split the dependencies of $\bar{k}(t)$ in Fig. 10 into two groups: first the clusters keep growing in time very rapidly, $B_0^* - B_3^*$; then, clearly, the growth slows down, just after the highest decay rate of M_z / M_s , $B_4^* - B_6^*$. This means, there is a critical value of an applied magnetic field such that for fields below this value the interparticle magnetic interactions manage to overpower Zeeman torques and keep particle magnetization mainly oriented in-plane; for higher fields the structural transformations are instead governed by B^* .

Bringing Figs. 12 and 13 together, one can conclude that both short-time response and the long-time evolution of the system are the results from a competition between Zeeman and dipolar forces, and depending on the one that dominates initially, the dynamics of the evolution changes from network-cluster-type behavior to a steel bead gas with small aggregates with vanishing magnetic moment.

IV. CONCLUSION

In this work we investigated a shaken mixture of glass and magnetized steel beads under the influence of an applied magnetic field, aligned perpendicular to the plane in which the particles are moving.

In the experiment, we reconfirmed a pattern evolution from chains to networks and more compact clusters, with a morphology similar to viscoelastic phase separation (VPS). Here the glass beads represent the fast phase, where the slow phase is formed by the steel beads, as soon they attach to each other. This pattern evolution is changed thoroughly by a vertically applied magnetic field, resulting in a third phase of solitary magnetic beads, as reflected by the large fraction of beads with zero number of neighbors. A convenient order parameter is the average number of neighbors. It shows for zero field a sigmoidal growth with apparent saturation. With increasing field its growth is more and more delayed. This is reflected by an exponential increase of the half-value period, i.e., the time

span at which half of the growth took place. The mechanism behind is the dipole-dipole repulsion of magnetized beads, which delays and eventually stops the cluster growth. Instead a phase of well-separated magnetic spheres emerges, which resembles a vortex glass [43,44].

In a simplistic coarse-grained simulation model, the time-dependent structural evolution was found to be in a qualitative agreement with the experiment for any value of the applied field. Particularly the average number of neighbors shows the same sigmoidal growth as found in the experiment. Moreover, the half-value periods of experiment and simulation increase exponentially with the field. As a result, the numerical approach was used to describe the long-time behavior. Here, for $t > 200$ simulation units a crossover to a different sigmoidal scaling regime was observed. It is particularly pronounced for the systems with more magnetic beads. Computer simulations were as well employed to analyze the magnetic properties of the system. The simulations revealed that in the first and the second time regimes, accessible both in simulation and experiment, the structural transformations tended to optimize dipolar interactions. Once the field is applied, immediately after quenching, all particles align with the applied field, providing the highest magnetization. After that, with the passage of time, the system’s magnetization follows a bi-logistic model, experiencing decay before eventually reaching saturation.

This change of behavior denotes a new time regime. In the long-time regime, accessible only in simulations, we observed that for low fields, whose values are presumably dependent on the magnetic particle concentration, the clusters keep growing, but the magnetization along the field direction only slowly decreases with time; for intermediate field values the growth of clusters is hindered and there is a strong competition between Zeeman and interparticle energies; finally, if the fields are high it seems that magnetization starts saturating as the only phase that remains is a magnetic particle gas; very few clusters that are found in this regime tend to have a vanishing dipole moment.

To conclude, by means of a magnetic field applied perpendicular to the plane of ferrogranulate one can very accurately control not only the morphology of the self-assembling clusters, but also the rate of evolution of the latter.

TABLE IV. The table displays the magnetic inductions B_n^* , impressed in the simulations, together with the parameters obtained by a fit of (6) (long-time regime) to the numerical data of $\bar{k}(t)$, displayed in Fig. 7.

B_n^*	(s.u.)	\bar{k}_{ini}	\bar{k}_{gro}	$t_{1/2}^*$ (s.u.)	p^*
B_0^*	0.0	1.86	3.00	5175.3	0.70
B_1^*	0.1	1.77	3.00	4467.6	0.69
B_2^*	0.2	2.19	1.49	3373.5	1.39
B_3^*	0.3	1.65	2.91	7176.0	0.58
B_4^*	0.4	2.03	1.09	3714.9	1.52
B_5^*	0.5	1.81	1.03	5619.4	1.26
B_6^*	0.6	1.62	0.42	4007.4	1.90
B_7^*	0.7	1.12	3.00	2665812.8	0.33
B_8^*	0.8	0.00	1.15	103.2	0.72

TABLE V. The table displays the magnetic inductions B_n^* , and the filling fractions used in the simulations, together with the parameters obtained by a fit of (6) to the short-time regime $t \in [5, 195]$ of the numerical data of $\bar{k}(t)$, displayed on the left-hand side of Fig. 11.

B_n^*	ϕ_g	ϕ_s	\bar{k}_{ini}	\bar{k}_{gro}	$t_{1/2}^*$ (s.u.)	p^*
B_0^*	0.05	0.15	0.56	1.76	8.5	0.8
	0.10	0.10	0.40	1.73	12.1	0.82
	0.15	0.05	0.19	1.76	30.92	0.75
B_5^*	0.05	0.15	0.57	1.35	11.6	1.0
	0.10	0.10	0.40	1.32	26.52	0.89
	0.15	0.05	0.22	1.17	158.4	0.81
B_8^*	0.05	0.15	0.55	0.81	39.6	0.99
	0.10	0.10	0.36	0.35	107.01	1.76
	0.15	0.05	0.08	0.49	574.02	37.37

ACKNOWLEDGMENTS

The authors would like to thank Klaus Oetter for constructions and K. Okrugin from the University of Vienna for technical support with production of the simulation data. The research was supported by the German-Austrian (D-A) fer-

TABLE VI. The table displays the magnetic inductions B_n^* , and the filling fractions used in the simulations, together with the parameters obtained by a fit of (6) to the long-time regime $t \in [744, 11744]$ of the numerical data of $\bar{k}(t)$, displayed on the right-hand side of Fig. 11.

B_n^*	ϕ_g	ϕ_s	\bar{k}_{ini}	\bar{k}_{gro}	$t_{1/2}^*$ (s.u.)	p^*
B_0^*	0.05	0.15	1.93	2.70	10000	0.54
	0.10	0.10	2.0	2.24	7454.23	0.81
	0.15	0.05	1.30	2.70	9325	0.56
B_5^*	0.05	0.15	1.93	0.88	4845	1.48
	0.10	0.10	1.49	1.60	10000	0.76
	0.15	0.05	0	3.25	9999	0.19
B_8^*	0.05	0.15	1.29	0.33	9608	2.00
	0.10	0.10	0.63	0.44	1000	0.67
	0.15	0.05	0.06	0.44	10000	1.17

rogranular research project funded by DFG (Ri 1054/7) and FWF (I5160).

APPENDIX

Tables IV–VI contain parameters obtained by fitting \bar{k} in Figs. 7 and 11 using Eq. (6).

- [1] R.-Y. Dong and S. Granick, Reincarnations of the phase separation problem, *Nat. Commun.* **12**, 911 (2021).
- [2] H. Tanaka, Viscoelastic phase separation, *J. Phys.: Condens. Matter* **12**, R207 (2000).
- [3] H. Tanaka, Y. Nishikawa, and T. Koyama, Network-forming phase separation of colloidal suspensions, *J. Phys.: Condens. Matter* **17**, L143 (2005).
- [4] H. Tanaka, Unusual phase separation in a polymer solution caused by asymmetric molecular dynamics, *Phys. Rev. Lett.* **71**, 3158 (1993).
- [5] H. Tanaka, Viscoelastic phase separation in biological cells, *Commun. Phys.* **5**, 167 (2022).
- [6] D. S. Lee, N. S. Wingreen, and C. P. Brangwynne, Chromatin mechanics dictates subdiffusion and coarsening dynamics of embedded condensates, *Nat. Phys.* **17**, 531 (2021).
- [7] J. W. Cahn, On spinodal decomposition, *Acta Metall.* **9**, 795 (1961).
- [8] K. G. Wilson, The renormalization group and critical phenomena, *Rev. Mod. Phys.* **55**, 583 (1983).
- [9] W. D. Callister and D. G. Rethwisch, *Materials Science and Engineering: An Introduction* (Wiley, New York, 2020).
- [10] D. L. Blair and A. Kudrolli, Clustering transitions in vibrofluidized magnetized granular materials, *Phys. Rev. E* **67**, 021302 (2003).
- [11] D. L. Blair and A. Kudrolli, *Magnetized granular materials*, in *The Physics of Granular Media* (Wiley, New York, 2004), pp. 281–296.
- [12] A. Kögel, P. A. Sánchez, R. Marezki, T. Dumont, E. S. Pyanzina, S. S. Kantorovich, and R. Richter, Coarsening dynamics of ferromagnetic networks—experimental results and simulations, *Soft Matter* **14**, 1001 (2018).
- [13] Z. M. Sherman and J. W. Swan, Transmutable colloidal crystals and active phase separation via dynamic, directed self-assembly with toggled external fields, *ACS Nano* **13**, 764 (2019).
- [14] P. A. Sánchez, J. Miller, S. S. Kantorovich, and R. Richter, Unknotting of quasi-two-dimensional ferrogranular networks by in-plane homogeneous magnetic fields, *J. Magn. Magn. Mater.* **499**, 166182 (2020).
- [15] O. Ashour, C. A. Rogers, and W. Kordonsky, Magnetorheological fluids: Materials, characterization and devices, *J. Intell. Mater. Syst. Struct.* **7**, 123 (1996).
- [16] C. Rinaldi, A. Chaves, S. Elborai, X. He, and M. Zahn, Magnetic fluid rheology and flows, *Curr. Opin. Colloid Interface Sci.* **10**, 141 (2005).
- [17] R. E. Rosensweig, *Ferrohydrodynamics* (Cambridge University Press, Cambridge, 1985).
- [18] S. Odenbach and S. Thurm, *Magnetoviscous Effects in Ferrofluids* (Springer, Berlin, 2002), pp. 185–201.
- [19] A. T. Skjeltorp, One- and two-dimensional crystallization of magnetic holes, *Phys. Rev. Lett.* **51**, 2306 (1983).
- [20] B. J. de Gans, N. J. Duin, D. van den Ende, and J. Mellema, The influence of particle size on the magnetorheological properties of an inverse ferrofluid, *J. Chem. Phys.* **113**, 2032 (2000).
- [21] R. Saldivar-Guerrero, R. Richter, I. Rehberg, N. Aksel, L. Heymann, and O. S. Rodriguez-Fernandez, Viscoelasticity of mono- and polydisperse inverse ferrofluids, *J. Chem. Phys.* **125**, 084907 (2006).

- [22] B. Smit, C. Williams, E. Hendriks, and S. D. Leeuw, Vapour-liquid equilibria for Stockmayer fluids, *Mol. Phys.* **68**, 765 (1989).
- [23] M. E. van Leeuwen and B. Smit, What makes a polar liquid a liquid?, *Phys. Rev. Lett.* **71**, 3991 (1993).
- [24] A. Z. Panagiotopoulos, Direct determination of fluid phase equilibria by simulation in the Gibbs ensemble: A review, *Mol. Simul.* **9**, 1 (1992).
- [25] M. J. Stevens and G. S. Grest, Coexistence in dipolar fluids in a field, *Phys. Rev. Lett.* **72**, 3686 (1994).
- [26] D. Adams and E. Adams, Static dielectric properties of the Stockmayer fluid from computer simulation, *Mol. Phys.* **42**, 907 (1981).
- [27] A. Jordan, R. Scholz, P. Wust, H. Föhling, and R. Felix, Magnetic fluid hyperthermia (MFH): Cancer treatment with AC magnetic field induced excitation of biocompatible superparamagnetic nanoparticles, *J. Magn. Magn. Mater.* **201**, 413 (1999).
- [28] P. J. Camp, J. C. Shelley, and G. N. Patey, Isotropic fluid phases of dipolar hard spheres, *Phys. Rev. Lett.* **84**, 115 (2000).
- [29] Y. Levin, What happened to the gas-liquid transition in the system of dipolar hard spheres? *Phys. Rev. Lett.* **83**, 1159 (1999).
- [30] C. Holm and J.-J. Weis, The structure of ferrofluids: A status report, *Curr. Opin. Colloid Interface Sci.* **10**, 133 (2005).
- [31] S. S. Kantorovich, A. O. Ivanov, L. Rovigatti, J. M. Tavares, and F. Sciortino, Nonmonotonic magnetic susceptibility of dipolar hard-spheres at low temperature and density, *Phys. Rev. Lett.* **110**, 148306 (2013).
- [32] L. Rovigatti, S. S. Kantorovich, A. O. Ivanov, J. M. Tavares, and F. Sciortino, Branching points in the low-temperature dipolar hard sphere fluid, *J. Chem. Phys.* **139**, 134901 (2013).
- [33] S. S. Kantorovich, A. O. Ivanov, L. Rovigatti, J. M. Tavares, and F. Sciortino, Temperature-induced structural transitions in self-assembling magnetic nanocolloids, *Phys. Chem. Chem. Phys.* **17**, 16601 (2015).
- [34] A. Smolla, S. S. Kantorovich, and R. Richter, Measuring the force in between susceptible dipolar hard spheres (unpublished).
- [35] A. Smolla, Messungen zur Anziehung zweier ferromagnetischer Stahlkugeln, bachelor's thesis, Universität Bayreuth, 2018.
- [36] Open Computer Vision (openCV), <https://github.com/opencv/opencv/wiki>
- [37] NetworkX: High-productivity software for complex networks, <https://networkx.github.io>
- [38] Python Software Foundation, <https://www.python.org>
- [39] A. Tsoularis and J. Wallace, Analysis of logistic growth models, *Math. Biosci.* **179**, 21 (2002).
- [40] J. J. Cerdà, S. Kantorovich, and C. Holm, Aggregate formation in ferrofluid monolayers: Simulations and theory, *J. Phys.: Condens. Matter* **20**, 204125 (2008).
- [41] A. Bródka, Ewald summation method with electrostatic layer correction for interactions of point dipoles in slab geometry, *Chem. Phys. Lett.* **400**, 62 (2004).
- [42] P. Meyer, Analysis of logistic growth models, *Technol. Forecast. Soc. Change* **47**, 89 (1994).
- [43] A. A. Abrikosov, Nobel lecture: Type-II superconductors and the vortex lattice, *Rev. Mod. Phys.* **76**, 975 (2004).
- [44] T. Nattermann and S. Scheidl, Vortex-glass phases in type-II superconductors, *Adv. Phys.* **49**, 607 (2000).
- [45] <https://doi.org/10.17605/OSF.IO/TFZDU>